

Università degli Studi di Bari Aldo Moro

FACOLTÀ DI SCIENZE MATEMATICHE, FISICHE E NATURALI

CORSO DI LAUREA MAGISTRALE IN FISICA

titolo

Relatore:

Dott.ssa Anna Colaleo

Laureando:

Filippo Errico

ANNO ACCADEMICO 2013-2014

Contents

1	The CMS detector at LHC	5
1.1	The Large Hadron Collider	5
1.2	The Compact Muon Solenoid	7
1.2.1	The tracking system	9
1.2.2	Electromagnetic calorimeter	12
1.2.3	Hadronic Calorimeter	14
1.3	Magnet	17
1.4	Muon System	18
	Bibliography	24

Chapter 1

The CMS detector at LHC

1.1 The Large Hadron Collider

Approved in the early '90s and started up in the 2008, the *Large Hadron Collider* (LHC) is currently the world's largest and most powerful particle accelerator.

Its main purpose is to help in testing the predictions of different theories of particle physics.

LHC [16], situated at the CERN laboratories of Geneva, is a proton-proton (pp) collider built to work at the design center of mass energy of $\sqrt{s} = 14$ TeV, with a bunch crossing every 25 ns and a design luminosity of 10^{34} cm $^{-2}$ s $^{-1}$. It is installed in the same circular underground tunnel occupied until the year 2000 by the Large Electron Positron collider (LEP). The pp collision are used, instead of the e^+e^- one of LEP, to reduce the synchrotron radiation, in order to accelerate the particles up to a very large energy. It was preferred to a $p\bar{p}$ collider because it allows to reach higher rate of events. In fact the low anti-proton production efficiency (10^5 protons are needed to create an anti-proton) and larger time needed to accumulate them, would make almost impossible to reach the high design luminosity of the LHC. The luminosity L is the parameter to quantify the performances of a collider, because the event rate R_i of a given process i , defined as the number of events occurring per unit of time, can be written as:

$$R_i = \frac{dN_i}{dt} = L \cdot \sigma_i \quad (1.1)$$

where σ_i is the cross section of the process i . The luminosity depends only on the machine parameters. Assuming a small crossing angle between the beams and Gaussian-shaped beam bunches, the luminosity L can be written as:

$$L = \frac{fn_b N^2}{4\pi\sigma^2} \quad (1.2)$$

where f is the revolution frequency of particle bunches, n_b is the number of bunches rotating in the accelerator, N is the number of protons in the two colliding bunches and σ is the RMS of beam profile distributions in the plane orthogonal to the beam direction.

In the LHC design, 1232 main dipole magnets (made of niobium-titanium super-conductor chilled with superfluid Helium at 1.9 K) generating a magnetic field up to 8.3 T, will be used to steer the particles into curvilinear trajectories. The two beams will run in two contiguous pipes with vacuum inside, separated by 19.4 cm, that will be unified in proximity of the interactions points, where the experiments will be placed. Because of the high luminosity of the LHC, large thermal power will be generated near the pipes due to the synchrotron radiation, making necessary the presence of a suitable cooling system. For this reason also the pipes will be in contact with superfluid Helium at 1.9 K.

In Figure 1.1 is shown the complete scheme of the accelerator chain of the LHC: the proton beam is created by using an electric field to pull the electrons from hydrogen atoms and start the acceleration. Protons are injected into the PS Booster (PSB) at an energy of 50 MeV from Linac2 (Linear Accelerator 2). The booster comprises four superposed rings: this is because at low energy intensity, the quality of the beams suffers from the repulsive forces between particles. By splitting up the injected beam this effect gets reduced. Once the beam reaches the energy of 1.4 GeV it is extracted and injected into Proton Synchrotron (PS). With a circumference of 628 m, the PS accelerates the beams up to 26 GeV when they are extracted and sent to the Super Proton Synchrotron (SPS). Built in the '70, the SPS has a length of 7 km. The beam is injected at 26 GeV, ramped up to 450 GeV and extracted to the LHC.

Once the energy-working point is reached, the beams are made to collide at four locations.

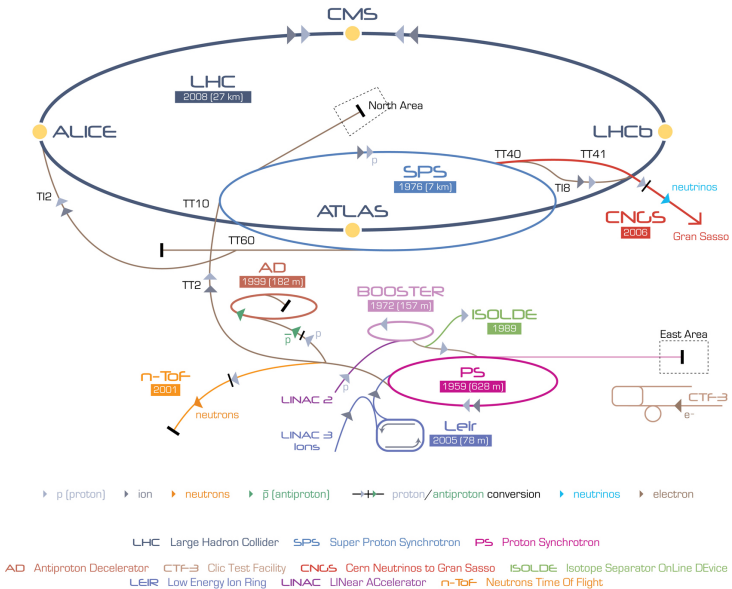


Figure 1.1: Accelerator scheme at CERN.

tions around the LHC, corresponding to the position of four particles detectors: ALICE (*A Large Ion Collider Experiment*), ATLAS (*A Toroidal LHC ApparatuS*), CMS (*Compact Muon Solenoid*) and LHCb (*Large Hadron Collider beauty*). In addition to these,

there are other three experiment installed at the LHC: TOTEM (*TOtal Elastic and diffractive cross section Measurement*) installed close to CMS, MoEDAL (*Monopole and Exotics Detector at the LHC*) close to LHCb and LHCf (*Large Hadron Collider forward*) near ATLAS.

The beams at LHC have a bunch structure as a direct consequence of the radio frequency acceleration scheme. Protons can only be accelerated when the RF field has the correct orientation when particles pass through an accelerating cavity. Under nominal operating conditions, each proton beam has 2808 bunches, with each bunch containing about 10^{11} protons. The bunch size is not constant around the ring getting squeezed as much as possible around the interaction points in order to increase the probability of collision. They measure a few centimetres long and a millimetre wide when they are far from a collision point; as the bunches approach the collision points, they are squeezed to about $20\ \mu\text{m}$. LHC uses a bunch spacing of 25 ns (or 7.5 m) corresponding to a frequency of 40 MHz.

In Table 1.1 are reported the designed LHC parameters and the ones reached at the end of RunII in 2018.

		Design	2018
Centre of mass energy	E	14 TeV	13 TeV
Luminosity	L	$10^{34}\ \text{cm}^{-2}\text{s}^{-1}$	—
Time spacing		25 ns	25 ns
Num. of bunches	k_B	2808	—
Num. protons per bunch	N_p	1.15×10^{11}	—

Table 1.1: LHC parameters

1.2 The Compact Muon Solenoid

The Compact Muon Solenoid (CMS) is one of the general purpose experiments which takes data at the LHC. Its physics goals range from the search for the Higgs boson to the searches for physics beyond the Standard Model, to the precision measurements of already known particles and phenomena [17].

The overall layout of CMS is shown in Figure 1.2. The inner tracker and the two calorimeters of CMS are located inside a 13 m-long, 5.9 m inner diameter, 3.8 T superconducting solenoid. In order to achieve good momentum resolution within a compact spectrometer without making stringent demands on muon-chamber resolution and alignment, a high magnetic field was chosen. The return field is large enough to saturate 1.5 m of iron, allowing four muon stations to be integrated to ensure robustness and full geometric coverage. The central part of CMS is called *barrel* while the two edges of the detector are denoted as *endcaps*. The tracking volume is given by a cylinder of length 5.8 m and diameter 2.6 m. In order to deal with high track multiplicities, CMS employs 10 layers

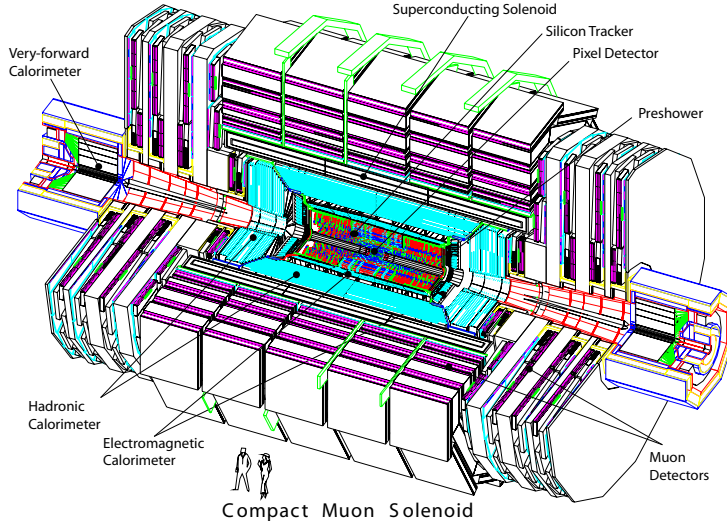


Figure 1.2: CMS detector overview.

of silicon microstrip detectors, which provide the required granularity and precision. In addition, 3 layers of silicon pixel detectors are placed close to the interaction region to improve the measurement of the impact parameter of charged-particle tracks, as well as the position of secondary vertexes. The electromagnetic calorimeter (ECAL) uses lead tungstate (PbWO_4) crystals with coverage in pseudorapidity up to $|\eta| < 3.0$. A preshower system is installed in front of the edges of ECAL for π^0 rejection.

Coordinate Conventions

The coordinate system adopted by CMS has the origin centered at the nominal collision point inside the experiment, the y -axis pointing vertically upward, and the x -axis pointing radially inward toward the center of the LHC. Thus, the z -axis points along the beam direction toward the Jura mountains from LHC Point 5. The azimuthal angle ϕ is measured from the x -axis in the x - y plane. The polar angle θ is measured from the z -axis. Pseudorapidity is defined as

$$\eta = -\ln \tan(\theta/2) \quad (1.3)$$

The value $\eta = 0$ corresponds to a direction perpendicular to the beamline, while the limit $\eta = \infty$ gives a direction parallel to the beamline. The momentum and energy measured transverse to the beam direction, denoted by p_T and E_T , respectively, are computed as follow:

$$p_T = p \sin\theta \quad (1.4)$$

$$E_T = E \sin\theta \quad (1.5)$$

Finally, particles which escape the detection leave an imbalance in the transverse plane which is quantified as missing transverse energy in the following way:

$$E_T^{miss} = - \sum_i p_T^i \quad (1.6)$$

as the negative vectorial sum of the transverse momentum of all the visible particles in the event.

1.2.1 The tracking system

The tracker [18, 19] , placed within the magnetic field, is the subdetector which is closer to the interaction point. It is dedicated to track and vertex finding. The silicon (Si) technology has been chosen for the whole tracker in order to provide good radiation hardness, high granularity and large hit redundancy to perform a good pattern recognition. The layout of the CMS tracker is shown in Figure 1.3. Close to the interaction vertex, in the barrel region, are 3 layers of hybrid pixel detectors at a radius (r) of about 4, 7 and 10 cm. The size of the pixel detector is $100 - 150 \text{ m}^2$. In the barrel part, the Si microstrip detectors are placed at r between 20 and 110 cm. The forward region has 2 pixel and 9 microstrip layers in each of the two endcaps. In order to avoid excessively shallow track crossing angles, the Inner Barrel is shorter than the Outer Barrel, and there are additional three Inner Disks in the transition region between barrel and endcaps, on each side of the Inner Barrel. The total area of the Si detectors is around 200 m^2 , providing a coverage up to $\eta = 2.5$. The material budget inside the active volume of the tracker increases from $0.4 \text{ radiation length } (X_0)$ at $\eta = 0$ to around $1 X_0$ at $|\eta| = 1.6$, before decreasing to $0.6 X_0$ at $|\eta| = 2.5$.

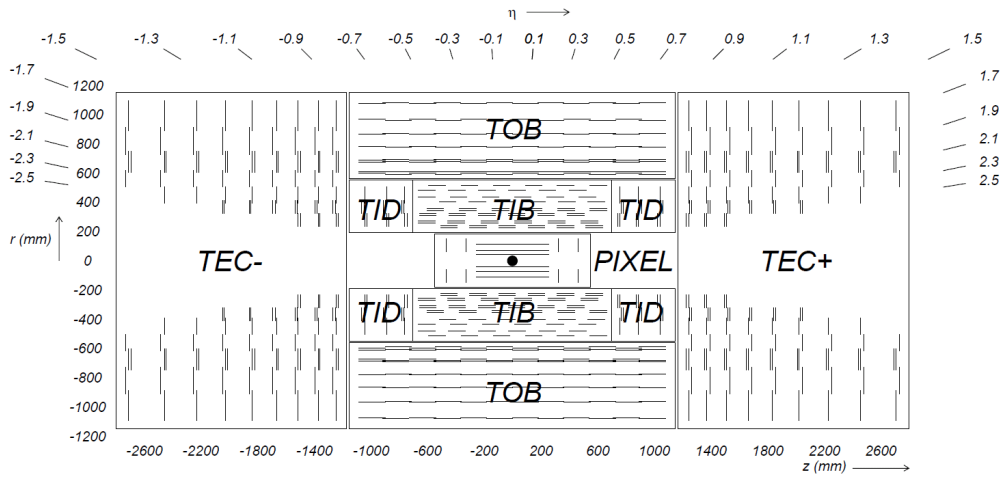


Figure 1.3: Schematic cross section through the CMS tracker in the $r - z$ plane: each line represents a detector module. Double lines indicate back-to-back modules which deliver stereo hits.

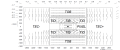


Figure 1.4: Material budget in units of radiation length as a function of pseudorapidity η for the different sub-detectors (left panel) and broken down into the functional contributions (right panel).

The pixel detector

The pixel system is the part of the tracking system that is closest to the interaction region and covers a pseudorapidity range $-2.5 < \eta < 2.5$, matching the acceptance of the central tracker. Figure 1.5 shows the geometric pixel structure. It contributes precise tracking points in $r - \phi$ and z and therefore is responsible for a small impact parameter resolution that is important for good secondary vertex reconstruction. With a pixel cell size of $100 \times 150 \mu\text{m}^2$ emphasis has been put on achieving similar track resolution in both $r - \phi$ and z directions: $10 \mu\text{m}$ in $r - \phi$ direction and $20 \mu\text{m}$ along z . The pixel detector is essential for the reconstruction of secondary vertices from b and tau decays, and forming seed tracks for the outer track reconstruction and high level triggering. It consists of three barrel layers (BPix) with two endcap disks (FPix). The 53-cm-long BPix layers will be located at mean radii of 4.4, 7.3 and 10.2 cm. The FPix disks, extending from ≈ 6 to 15 cm in radius, will be placed on each side at $z = \pm 34.5$ and $z = \pm 46.5$ cm. BPix (FPix) contain 48 million (18 million) pixels covering a total area of 0.78 (0.28) m^2 . The arrangement of the 3 barrel layers and the forward pixel disks on each side gives 3 tracking points over almost the full η range. In the high η region the 2 disk points are combined with the lowest possible radius point from the 4.4 cm barrel layer.

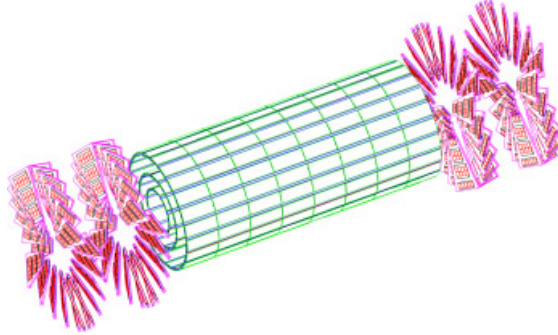


Figure 1.5: Geometrical layout of the pixel detector.

Pixel Upgrade

Due to the radiation damage and significant data losses due to high occupancy in the readout chip of the pixel detector, the pixel system has been replaced by a new one in the end-of-year shutdown during winter 2016/2017 in order to maintain the excellent

tracking and other physics performances [20]. The main new features of the upgraded pixel detector are a ultra-light mechanical design with four barrel layers and three end-cap disks, digital readout chip with higher rate capability and a new cooling system. The geometrical layout of the upgrade system, shown in Figure 1.6, consists of four

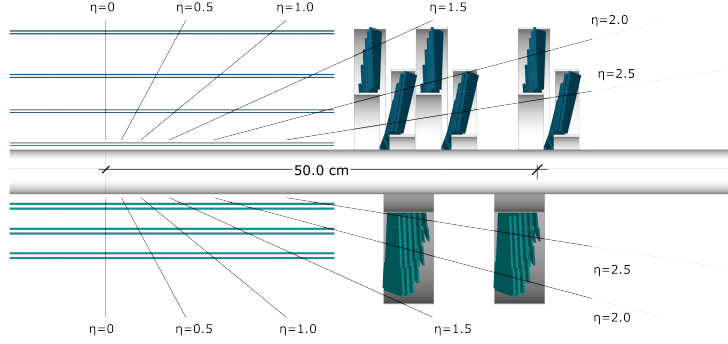


Figure 1.6: Comparison of the geometrical layouts of the old (bottom) and upgraded (top) CMS pixel detectors.

cylindrical barrel layers placed at radii of 29, 68, 109, 160 mm and three disks in each of the forward regions placed at a distance from the nominal interaction point of 291, 396 and 516 mm. This layout is optimized in order to offer full 4-hit tracking coverage up to pseudorapidities of 2.5, with an increased redundancy compared to the present system.

The silicon strip detector

The silicon strip detector is composed of three different subsystem. The Tracker Inner Barrel and Disks (TIB/TID see Figure 1.3) are composed of 4 barrel layers, supplemented by 3 disks at each end. TIB/TID delivers up to 4 $r - \phi$ measurements on a trajectory using $320\ \mu m$ thick silicon microstrip sensors with their strips parallel to the beam axis in the barrel and radial on the disks. The strip pitch is $80\ \mu m$ on layers 1 and 2 and $120\ \mu m$ on layers 3 and 4 in the TIB, leading to a single point resolution of $23\ \mu m$ and $35\ \mu m$, respectively. In the TID the mean pitch varies between $100\ \mu m$ and $141\ \mu m$. The TIB/TID is surrounded by the Tracker Outer Barrel (TOB). It has an outer radius of 116 cm and consists of 6 barrel layers of $500\ \mu m$ thick microstrip sensors with strip pitches of $183\ \mu m$ on the first 4 layers and $122\ \mu m$ on layers 5 and 6. It provides another 6 $r - \phi$ measurements with single point resolution of $53\ \mu m$ and $35\ \mu m$, respectively. The TOB extends in z between ± 118 cm. Beyond this z range the Tracker EndCaps (\pm TEC, where the sign indicates the location along the z axis) cover the region $124\text{ cm} < |z| < 282\text{ cm}$ and $22.5\text{ cm} < |r| < 113.5\text{ cm}$. Each TEC is composed of 9 disks, carrying up to 7 rings of silicon microstrip detectors ($320\ \mu m$ thick on the inner 4 rings, $500\ \mu m$ thick on rings 5-7) with radial strips of $97\ \mu m$ to $184\ \mu m$ average pitch. Thus, they provide up to 9 ϕ measurements per trajectory. In addition, the modules in the first two layers and

rings, respectively, of TIB, TID, and TOB as well as rings 1, 2, and 5 of the TECs carry a second microstrip detector module which is mounted back-to-back with a stereo angle of 100 mrad in order to provide a measurement of the second coordinate (z in the barrel and r on the disks). The achieved single point resolution of this measurement is $230\mu\text{m}$ and $530\mu\text{m}$ in TIB and TOB, respectively, and varies with pitch in TID and TEC.

The sensor elements in the strip tracker are single sided p-on-n type silicon micro-strip sensors shown in Figure 1.7: in TIB/TID and on the inner 4 rings of the TECs, thin sensors of $(320 \pm 20) \mu\text{m}$ wafer thickness are used, with substrate resistivity of $ro = 1.55 - 3.25 \text{ k}\Omega\text{cm}$; TOB and the outer 3 rings of the TECs are equipped with thicker sensors of $(500 \pm 20) \mu\text{m}$ thickness, with substrate resistivity of $ro = 4 - 8 \text{ k}\Omega\text{cm}$.

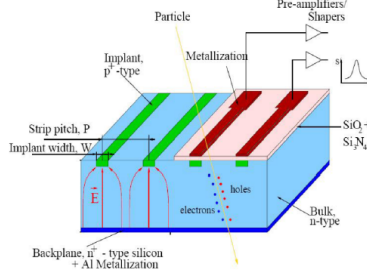


Figure 1.7: Single sided p-on-n type silicon micro-strip sensor.

LASER ALIGNMENT SYSTEM

1.2.2 Electromagnetic calorimeter

The electromagnetic calorimeter plays an essential role in the study of the physics of electroweak symmetry breaking, and in the exploration of beyond the Standard Model scenarios. ECAL is a homogeneous calorimeter of almost 76000 Lead Tungstate PbWO_4 scintillating crystals divided into a barrel and two endcaps. A 3D view of the barrel and endcap electromagnetic calorimeter is shown in Figure 1.8.

The Barrel Calorimeter

The barrel part of the ECAL covers the pseudorapidity range $|\eta| < 1.479$. The front face of the crystals is at a radius of 1.29 m and each crystal has a square cross-section of $22 \times 22 \text{ mm}^2$ and a length of 230 mm corresponding to $25.8 X_0$. The truncated pyramid-shaped crystals are mounted in a geometry which is off-pointing with respect to the mean position of the primary interaction vertex, with a 3° tilt in both ϕ and in η . The crystal cross-section corresponds to $\Delta\eta \times \Delta\phi = 0.0175 \times 0.0175$ (1°). The barrel granularity is 360-fold in ϕ and (2×85) -fold in η , resulting in a total number of 61 200 crystals. The crystal volume in the barrel amounts to 8.14 m^3 (67.4 t). Crystals for each half-barrel are grouped in 18 supermodules each subtending 20° in ϕ . Each supermodule comprises four modules with 500 crystals in the first module and 400 crystals in each of the remaining three modules. For simplicity of construction and assembly, crystals have

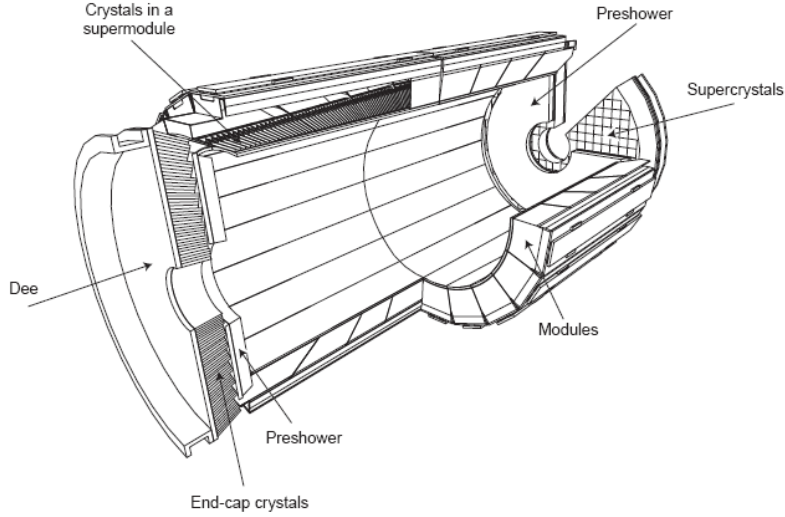


Figure 1.8: A 3D view of the electromagnetic calorimeter.

been grouped in arrays of 2×5 crystals which are contained in a very thin wall ($200 \mu\text{m}$) alveolar structure and form a submodule. Thermal regulation is carried out by two active systems: 1) a specially regulated cooling circuit which keeps the operating temperature (ambient temperature) of the crystal array and of the APDs within a tight temperature spread of $\pm 0.05^\circ\text{C}$, ensuring adequate thermal stability; 2) the power cooling circuit evacuates the heat generated by all power sources in the supermodule (each supermodule is designed as a separate thermal entity).

The Endcap Calorimeter

The endcap part of the crystal calorimeter covers a pseudorapidity range from 1.48 to 3.0. The design of the endcaps provides precision energy measurement up to $|\eta| = 2.5$. Crystals are however installed up to $|\eta| = 3$ in order to augment the energy-flow measurement in the forward direction. The mechanical design of the endcap calorimeter is based on an offpointing pseudo-projective geometry using tapered crystals of the same shape and dimensions ($24.7 \times 24.7 \times 220 \text{ mm}^3$) grouped together into units of 36, referred to as supercrystals. A total of 268 identical supercrystals is used to cover each endcap with a further 64 sectioned supercrystals used to complete the inner and outer perimeter. Each endcap contains 7324 crystals, corresponding to a volume of 1.52 m^3 (12.6 t). Both endcaps are identical. Each endcap detector is constructed using Dee-shaped sections. Because of the high radiation levels in the endcaps all materials used in this region must tolerate very large doses and neutron fluences.

The endcap part also includes the preshower detector.

The Preshower Detector

The endcap preshower covers a pseudorapidity range from $|\eta| = 1.65$ to 2.61 . Its main function is to provide π^0 - γ separation. The preshower detector, placed in front of the crystals, contains two lead converters of a total thickness of $2 X_0$ and $1 X_0$ respectively, followed by detector planes of silicon strips with a pitch of < 2 mm. The impact position of the electromagnetic shower is determined by the center-of-gravity of the deposited energy. The accuracy is typically $300 \mu\text{m}$ at 50 GeV. In order to correct for the energy deposited in the lead converter, the energy measured in the silicon is used to apply corrections to the energy measurement in the crystal. The fraction of energy deposited in the preshower (typically 5% at 20 GeV) decreases with increasing incident energy.

Energy Resolution

For the energy range of about 25 GeV to 500 GeV, the ECAL energy resolution has been parameterized as:

$$\frac{\sigma(E)}{E} = \frac{a}{\sqrt{E}} \oplus \frac{\sigma_n}{E} \oplus c \quad (\text{E in GeV}) \quad (1.7)$$

where a is the stochastic term, σ_n the noise, and c the constant term. Figure 1.9 summarizes the different contributions expected for the energy resolution. Terms representing the degradation of the energy resolution at extremely high energies have not been included. The stochastic term includes fluctuations in the shower containment as well as a contribution from photostatistics. The noise term contains the contributions from electronic noise and pile-up energy; the former is quite important at low energy, the latter is negligible at low luminosity. The curve labeled *intrinsic* includes the shower containment and a constant term of 0.55%. The constant term must be kept down to this level in order to profit from the excellent stochastic term of PbWO₄ in the energy range relevant for the search for new physics. To achieve this goal, in situ calibration/monitoring using isolated high p_T electrons is performed.

1.2.3 Hadronic Calorimeter

Figure 1.10 shows the longitudinal view of the CMS detector with the locations od the hadron calorimeters [22]. The dashed lines are at fixed η values. The hadron calorimeter barrel and endcaps sit behind the tracker and the electromagnetic calorimeter as seen from the interaction point. The hadron calorimeter barrel is radially restricted between the outer extent of the electromagnetic calorimeter ($R = 1.77$ m) and the inner extent of the magnet coil ($R = 2.95$ m). This constrains the total amount of material which can be put in to absorb the hadronic shower. Therefore, an outer hadron calorimeter or tail catcher is placed outside the solenoid complementing the barrel calorimeter. Beyond $|\eta| = 3$, the forward hadron calorimeters placed at 11.2 m from the interaction point extend the pseudorapidity coverage down to $|\eta| = 5.2$ using a Cherenkov-based, radiation-hard technology.

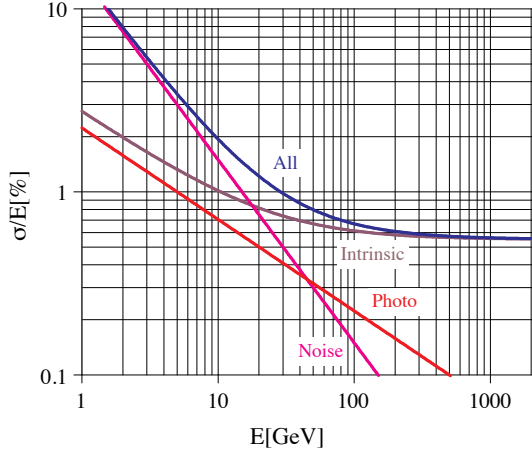


Figure 1.9: Different contributions to the energy resolution of the PbWO_4 calorimeter.

Hadron barrel (HB)

The HB is a sampling calorimeter covering the pseudorapidity range $|\eta| < 1.3$. It is divided into two half-barrel sections, each half-section being inserted from either end of the barrel cryostat of the superconducting solenoid and subsequently hung from rails in the median plane. The HB consists of 36 identical azimuthal wedges which form the two half-barrels (HB+ and HB-). The wedges are constructed out of flat brass absorber plates aligned parallel to the beam axis. Each wedge is segmented into four azimuthal angle (ϕ) sectors. The plates are bolted together in a staggered geometry resulting in a configuration that contains no projective dead material for the full radial extent of a wedge. The innermost and outermost plates are made of stainless steel for structural strength. The plastic scintillator is divided into 16 η sectors, resulting in a segmentation $(\Delta\eta, \Delta\phi) = (0.087, 0.087)$. The wedges are themselves bolted together, in such a fashion as to minimize the crack between the wedges to less than 2 mm. The absorber consists of a 40-mm-thick front steel plate, followed by eight 50.5- mm-thick brass plates, six 56.5-mm-thick brass plates, and a 75-mm-thick steel back plate. The total absorber thickness at 90° is 5.82 interaction lengths (λ_I). The HB effective thickness increases with polar angle (θ) as $1/\sin\theta$, resulting in $10.6 \lambda_I$ at $|\eta| = 1.3$. The electromagnetic crystal calorimeter in front of HB adds about $1.1 \lambda_I$ of material.

Hadron endcap (HE)

The hadron calorimeter endcaps (HE) cover a substantial portion of the rapidity range, $1.3 < |\eta| < 3$. Since the calorimeter is inserted into the ends of a 4-T solenoidal magnet, the absorber must be made from a non-magnetic material in order not to distort it. It must also have a maximum number of interaction lengths to contain hadronic showers, good mechanical properties and reasonable cost, leading to the choice of C26000 cartridge brass. The endcaps are attached to the muon endcap yoke. Only a small part of



Figure 1.10: Longitudinal view of the CMS detector showing the locations of the hadron barrel (HB), endcap (HE), outer (HO) and forward (HF) calorimeters.

the calorimeter structure can be used for the fixation to the magnet iron, because the majority of the space between HE and muon absorber is occupied with muon cathode strip chambers. A 10-t electromagnetic calorimeter (EE) with a 2-t preshower detector (ES) is attached at the front face of HE. The design of the absorber is driven by the need to minimize the cracks between HB and HE, rather than single-particle energy resolution, since the resolution of jets in HE will be limited by pileup, magnetic field effects, and parton fragmentation. The plates are bolted together in a staggered geometry resulting in a configuration that contains no projective dead material. The design provides a self-supporting hermetic construction. The brass plates are 79-mm-thick with 9-mm gaps to accommodate the scintillators. The total length of the calorimeter, including electromagnetic crystals, is about $10 \lambda_I$. The granularity of the calorimeters is $\Delta\eta \times \Delta\phi = 0.087 \times 0.087$ for $|\eta| < 1.6$ and $\Delta\eta \times \Delta\phi \approx 0.17 \times 0.17$ for $|\eta| \geq 1.6$.

Hadron outer (HO)

In the central pseudorapidity region, the combined stopping power of EB plus HB does not provide sufficient containment for hadron showers. To ensure adequate sampling depth for $|\eta| < 1.3$, the hadron calorimeter is extended outside the solenoid with a tail catcher called the HO or outer calorimeter. The HO utilises the solenoid coil as an additional absorber equal to $1.4/\sin\theta$ interaction lengths and is used to identify late starting showers and to measure the shower energy deposited after HB. Outside the vacuum tank of the solenoid, the magnetic field is returned through an iron yoke designed in the form of five 2.536 m wide (along z-axis) rings. The HO is placed as the first sensitive layer in each of these five rings; the nominal central z positions of the five rings are respectively -5.342 m, -2.686 m, 0, $+2.686$ m and $+5.342$ m. At $\eta = 0$, HB has the minimal absorber depth. Therefore, the central ring (ring 0) has two layers of

HO scintillators on either side of a 19.5 cm thick piece of iron (the tail catcher iron) at radial distances of 3.82 m and 4.07 m, respectively. All other rings have a single HO layer at a radial distance of 4.07 m. The total depth of the calorimeter system is thus extended to a minimum of $11.8 \lambda_I$ except at the barrel-endcap boundary region. The HO is constrained by the geometry of the muon system. The segmentation of these detectors closely follows that of the barrel muon system. Each ring has 12 identical ϕ -sectors. The 12 sectors are separated by 75-mm-thick stainless steel beams which hold successive layers of iron of the return yoke as well as the muon system.

Hadron foward (HF)

The forward calorimeter is a cylindrical steel structure with an outer radius of 130.0 cm. The front face of the calorimeter is located at 11.2 m from the interaction point. The hole for the beam pipe is cylindrical, with radius 12.5 cm from the center of the beam line. This structure is azimuthally subdivided into 20° modular wedges. Thirty-six such wedges (18 on either side of the interaction point) make up the HF calorimeters. The fibres run parallel to the beam line, and are bundled to form 0.175×0.175 ($\Delta\eta \times \Delta\phi$) towers. The detector is housed in a hermetic radiation shielding which consists of layers of 40 cm thick steel, 40 cm of concrete, and 5 cm of polyethylene. A large plug structure in the back of the detector provides additional shielding. It consists of a steel absorber structure that is composed of 5 mm thick grooved plates. Fibres are inserted in these grooves. The detector is functionally subdivided into two longitudinal segments. Half of the fibres run over the full depth of the absorber (165 cm $\approx 10 \lambda_I$) while the other half starts at a depth of 22 cm from the front of the detector. These two sets of fibres are read out separately. This arrangement makes it possible to distinguish showers generated by electrons and photons, which deposit a large fraction of their energy in the first 22 cm, from those generated by hadrons, which produce nearly equal signals in both calorimeter segments on average. The long fibre section is referred as L (measuring the total signal), and the short fibre section as S (measuring the energy deposition after 22 cm of steel). The absorber has grooves which make a square grid separated by 5.0 ± 0.1 mm center-to-center. Long and short fibres alternate in these grooves. The packing fraction by volume (fibre/total) in the first 22 cm is 0.57% and is twice as large beyond that depth.

1.3 Magnet

The required performance of the muon system, and hence the bending power, is defined by the narrow states decaying into muons and by the unambiguous determination of the sign for muons with a momentum of 1 TeV/c. This requires a momentum resolution of $\Delta p/p \sim 10\%$ at $p = 1$ TeV. To achieve this goal, CMS chose a large superconducting solenoid, the parameters of which are given in table 1.2.

Parameter	Value
Field	3.8 T
Inner bore	5.9 m
Length	12.9 m
Number of turns	2168
Current	19.5 kA
Stored energy	2.7 GJ

Table 1.2: Parameters of the CMS superconducting solenoid.

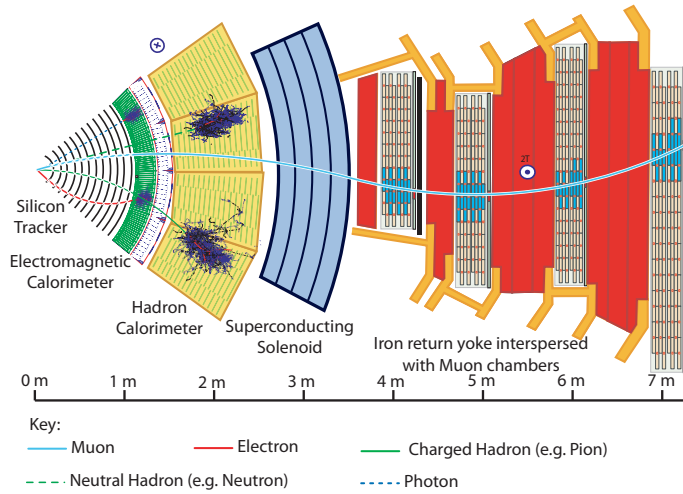


Figure 1.11: Schematic view of a transverse slice of the central part of the CMS detector.

1.4 Muon System

The muon system is the outermost of the CMS subdetectors. Its main goals are the identification of muons, thanks to their high penetrating power, and a precise measurement of their momentum, with the help of the information coming from the tracker. The muon system also works as trigger for events which involve muons and it provides a precise time measurement of the bunch crossing. The CMS muon system [23] relies on three kinds of gaseous detectors: drift tubes (DT), cathode strip chambers (CSC) and resistive plate chambers (RPC). The DT and the CSC provide an excellent spatial resolution for the measurement of charged particle momentum; the RPC are used for trigger issues because of the very good timing. The active parts of the muon system are hosted into stations which are interleaved by the iron layers of the return yoke of the magnet. The longitudinal view of a quarter of the muon system is given in Figure 1.12. The barrel extends up to $|\eta| < 1.4$, the endcaps up to $|\eta| < 2.4$.

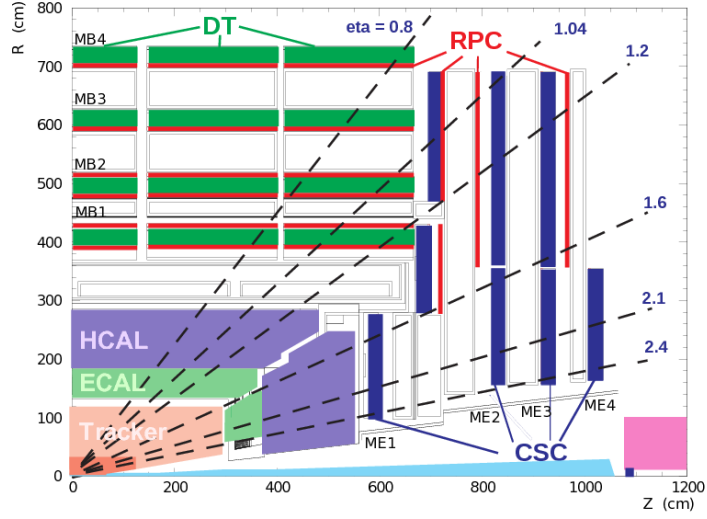


Figure 1.12: Longitudinal view of one quarter of the CMS muon system

DT

The CMS barrel muon detector consists of 4 stations forming concentric cylinders around the beam line: the 3 inner cylinders have 60 drift chambers each and the outer cylinder has 70. It is possible to use drift chambers as the tracking detectors for the barrel muon system because of the low expected rate and the relatively low strength of the local magnetic field. In each of the 12 sectors of the yoke there are 4 muon chambers per wheel, labeled MB1, MB2, MB3, and MB4, Figure 1.13. The yoke-iron supports that are between the chambers of a station generate 12 unavoidable dead zones in the ϕ coverage, although the supports are placed so as not to overlap in ϕ . A DT chamber is made of 3 (or 2) superlayers (SL, see Figure 1.14), each made of 4 layers of rectangular drift cells staggered by half a cell. The SL is the smallest independent unit of the design. The wires in the 2 outer SLs are parallel to the beam line and provide a track measurement in the magnetic bending plane ($r-\phi$). In the inner SL, the wires are orthogonal to the beam line and measure the z position along the beam. This third, z -measuring, SL is not present in the fourth station, which therefore measures only the ϕ coordinate. The main element in the DT is the drift cell, shown in Figure 1.15: its pitch is 42 mm, while the layer pitch is 13 mm. The gas used is Ar – CO₂ mixture (85 % - 15 %).

CSC

CMS Endcap Muon system consists of Cathode Strip Chambers (CSC) arranged in 4 stations (ME1, ME2, ME3, ME4) (Figure 1.16). The chambers are trapezoidal and cover either 10° or 20° in ϕ ; all chambers, except for the ME1/3 ring, overlap and provide contiguous ϕ -coverage. A muon in the pseudorapidity range $1.2 < |\eta| < 2.4$ crosses 3 or 4 CSCs. In the endcap-barrel overlap range, $0.9 < |\eta| < 1.2$, muons are

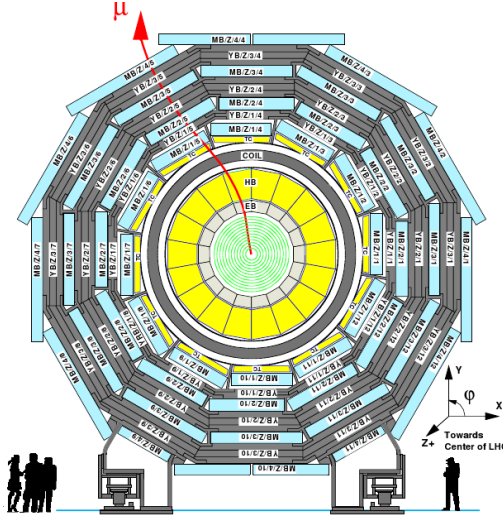


Figure 1.13: Layout of the CMS barrel muon DT chambers in one of the 5 wheels. The chambers in each wheel are identical with the exception of wheels -1 and +1 where the presence of cryogenic chimneys for the magnet shortens the chambers in 2 sectors. Note that in sectors 4 (top) and 10 (bottom) the MB4 chambers are cut in half to simplify the mechanical assembly and the global chamber layout.

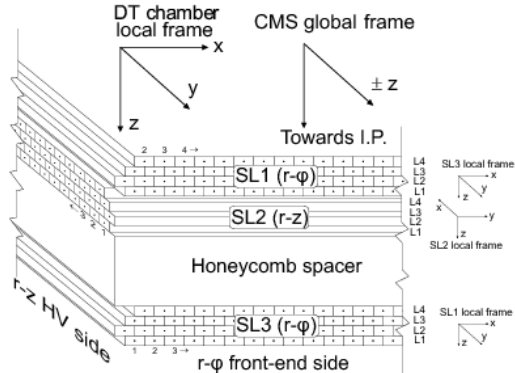


Figure 1.14: Layout of the DT chamber: each chamber is made of 3 Superlayers of Drift Tube and each SL is made of 4 layers of Drift Tube.

detected by both the barrel drift tubes (DT) and endcap CSCs. The CSCs are multiwire proportional chambers comprised of 6 anode wire planes interleaved among 7 cathode panels (Figure ??). Wires run azimuthally and define a track's radial coordinate. Strips are milled on cathode panels and run lengthwise at constant $\Delta\phi$ width. The largest chambers, ME2/2 and ME3/2, are about $3.4 \times 1.5 \text{ m}^2$ in size. The overall area covered by the sensitive planes of all chambers is about 5000 m^2 , the gas volume is $\sim 50 \text{ m}^3$, and the number of wires is about 2 million. There are about 9000 high-voltage channels in the

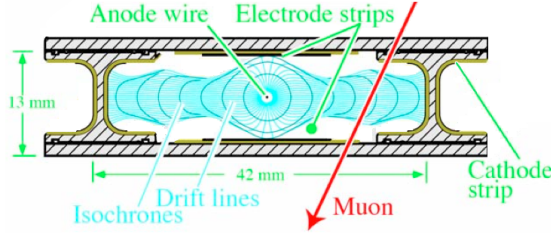


Figure 1.15: Sketch of a cell showing drift lines and isochrones. The plates at the top and bottom of the cell are at ground potential. The voltages applied to the electrodes are +3600V for wires, +1800V for strips, and -1200V for cathodes.

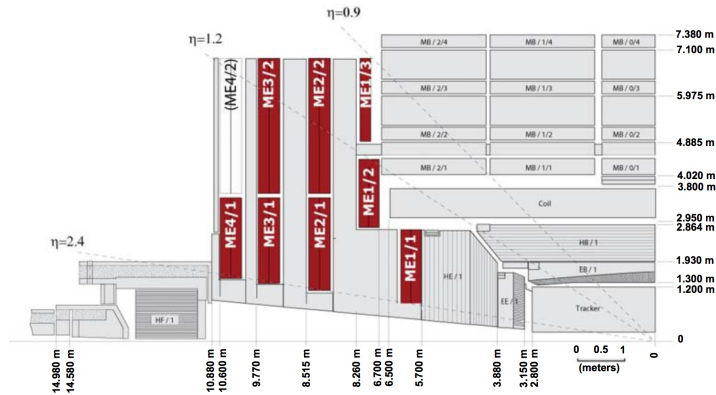


Figure 1.16: Quarter-view of the CMS detector. Cathode strip chambers of the Endcap Muon system are highlighted.

system, about 220 000 cathode strip read-out channels with 12-bit signal digitisation, and about 180 000 anode wire read-out channels. The CSCs provide the functions of precision muon measurement and muon trigger in one device. The nominal gas mixture used is 40%Ar + 50%CO₂ + 10%CF₄.

RPC

Resistive Plate Chambers (RPC) are gaseous parallel-plate detectors that combine adequate spatial resolution with a time resolution comparable to that of scintillators. An RPC is capable of tagging the time of an ionising event in a much shorter time than the 25 ns between 2 consecutive LHC bunch crossings (BX). The CMS RPC basic double-gap module consists of 2 gaps, hereafter referred as up and down gaps, operated in avalanche mode with common pick-up read-out strips in between. The total induced signal is the sum of the 2 single-gap signals. Six layers of RPC chambers are embedded in the barrel iron yoke, 2 located in each of the first and second muon stations and 1 in each of the 2 last stations. The redundancy in the first 2 stations allows the trigger

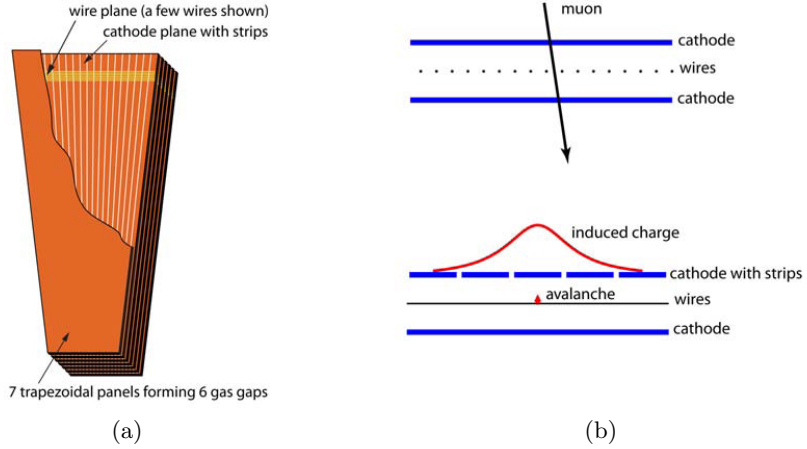


Figure 1.17: (a) Layout of a CSC made of 7 trapezoidal panels. The panels form 6 gas gaps with planes of sensitive anode wires. (b) A schematic view of a single gap illustrating the principle of CSC operation. By interpolating charges induced on cathode strips by avalanche positive ions near a wire, one can obtain a precise localisation of an avalanche along the wire direction.

algorithm to perform the reconstruction always on the basis of 4 layers, even for low p_T particles, which may stop inside the iron yoke. In the endcap region, 3 layers up to $\eta = 1.6$ are built. In the barrel iron yoke, the RPC chambers form 6 coaxial sensitive cylinders (all around the beam axis) that are approximated with concentric dodecagon arrays arranged into 4 stations (Figure 1.18). In the first and second muon stations there are 2 arrays of RPC chambers located internally and externally with respect to the Drift Tube (DT) chambers: RB1in and RB2in at smaller radius and RB1out and RB2out at larger radius. In the third and fourth stations there are again 2 RPC chambers, both located on the inner side of the DT layer (named RB3+ and RB3-, RB4+ and RB4-). A special case is RB4 in sector 4, which consists of 4 chambers: RB4++, RB4+, RB4-, and RB4-. Finally, in sectors 9 and 11 there is only 1 RB4 chamber. In the forward and backward regions of the CMS detector, 3 iron disks constitute the endcap yokes.

GEM

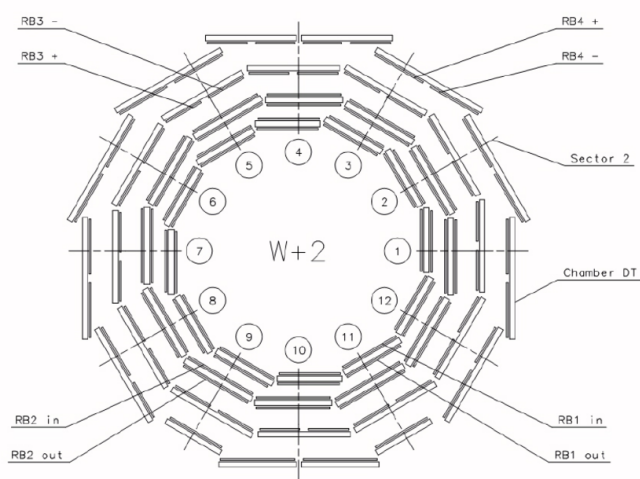


Figure 1.18: Schematic layout of one of the 5 barrel wheels, which are labeled ?2, ?1, 0, +1, and +2, respectively. Each wheel is divided into 12 sectors that are numbered as shown.

Bibliography

- [1] C. Patrignani et al. (Particle Data Group), Chin. Phys. C, 40, 100001 (2016) and 2017 update.
- [2] Halzen and Martin, *Quarks and Leptons: An Introductory Course in Modern Particle Physics*, John Wiley & Sons (1984).
- [3] M.E.Peskin and D.V.Schroeder, *An Introduction To Quantum Field Theory*, Addison-Wesley, 1995.
- [4] M.Maggiore, *A Modern Introduction to Quantum Filed Theory*, Oxford University Press, 2004.
- [5] A.Pich, *The standard model of electroweak interactions*, arXiv:hep-ph/0502010v, 2005.
- [6] UA1 Collaboration, *Experimental observation of isolated large transverse energy electrons with associated missing energy at $\sqrt{s} = 540 \text{ GeV}$* .
- [7] UA1 Collaboration, *Experimental observation of lepton pairs of invariant mass around $95 \text{ GeV}/c^2$ at the CERN SPS collider*.
- [8] S. Weinberg, *A model of leptons*, Phys. Rev. Lett. 19 (1967) 1264.
- [9] MuLan Collaboration, *Improved Measurement of the Positive Muon Lifetime and Determination of the Fermi Constant*, Phys.Rev.Lett.99:032001,2007, arXiv:0704.1981.
- [10] ATLAS Collaboration, *Observation of a new particle in the search for the Standard Model Higgs boson with the ATLAS detector at the LHC*, Phys.Lett. B716 (2012), pp. 1-29, DOI: 10.1016/j.physletb.2012.08.020.
- [11] CMS Collaboration, *Observation of a new boson at a mass of 125 GeV with the CMS experiment at the LHC*, Physics Letters B716 (2012), pp. 30-61. DOI: <http://dx.DOI.org/10.1016/j.physletb.2012.08.021> .
- [12] LHC Higgs Cross Section Working Group,
<https://twiki.cern.ch/twiki/bin/view/LHCPhysics/LHCHXSWG>.

- [13] D. de Florian et al., [LHC Higgs Cross Section Working Group], CERN-2017-002-M, arXiv:1610.07922[hep-ph] (2016).
- [14] S. Heinemeyer et al., [LHC Higgs Cross Section Working Group], CERN?2013?004, arXiv:1307.1347 [hep-ph] (2013).
- [15] D. de Florian et al., [LHC Higgs Cross Section Working Group], CERN?2017?002-M, arXiv:1610.07922[hep-ph] (2016).
- [16] Lyndon Evans and Philip Bryant, [LHC Machine], 1748-0221-3-08-S08001, Journal of Instrumentation (2008), <http://stacks.iop.org/1748-0221/3/i=08/a=S08001>
- [17] CMS collaboration, [The Compact Muon Solenoid technical proposal], CERN-LHCC-94-38, <http://cdsweb.cern.ch/record/290969>
- [18] CMS collaboration, [The CMS tracker system project: technical design report], CERN-LHCC-98-006, <http://cdsweb.cern.ch/record/368412>.
- [19] CMS collaboration, [The CMS tracker: addendum to the technical design report] CERN-LHCC-2000-016, <http://cdsweb.cern.ch/record/490194>.
- [20] Anirban Saha, [Phase 1 upgrade of the CMS pixel detector], Journal of Instrumentation (2017), <http://stacks.iop.org/1748-0221/12/i=02>
- [21] PARTICLE DATA GROUP collaboration, S. Eidelman et al., [Review of particle physics] Phys. Lett. B 592 (2004) 1.
- [22] CMS collaboration, [The hadron calorimeter project: technical design report], CERN-LHCC-97-031, <http://cdsweb.cern.ch/record/357153>.
- [23] CMS collaboration, [The CMS muon project, technical design report], CERN-LHCC-97-032, <http://cdsweb.cern.ch/record/343814>.